Refinements to Ice Particle Mass Dimensional and Terminal Velocity Relationships for Ice Clouds. Part II: Evaluation and Parameterizations of Ensemble Ice Particle Sedimentation Velocities

ANDREW J. HEYMSFIELD

National Center for Atmospheric Research, Boulder, Colorado*

GERD-JAN VAN ZADELHOFF AND DAVID P. DONOVAN

Koninklijk Nederlands Meteorologisch Instituut, De Bilt, Netherlands

FREDERIC FABRY

Department of Atmospheric and Oceanic Sciences, and McGill School of Environment, McGill University, Montreal, Quebec, Canada

ROBIN J. HOGAN AND ANTHONY J. ILLINGWORTH

Department of Meteorology, University of Reading, Reading, United Kingdom

(Manuscript received 10 April 2006, in final form 9 August 2006)

ABSTRACT

This two-part study addresses the development of reliable estimates of the mass and fall speed of single ice particles and ensembles. Part I of the study reports temperature-dependent coefficients for the mass-dimensional relationship, $m = aD^b$, where D is particle maximum dimension. The fall velocity relationship, $V_t = AD^B$, is developed from observations in synoptic and low-latitude, convectively generated, ice cloud layers, sampled over a wide range of temperatures using an assumed range for the exponent b. Values for a, A, and B were found that were consistent with the measured particle size distributions (PSD) and the ice water content (IWC).

To refine the estimates of coefficients a and b to fit both lower and higher moments of the PSD and the associated values for A and B, Part II uses the PSD from Part I plus coincident, vertically pointing Doppler radar returns. The observations and derived coefficients are used to evaluate earlier, single-moment, bulk ice microphysical parameterization schemes as well as to develop improved, statistically based, microphysical relationships. They may be used in cloud and climate models, and to retrieve cloud properties from ground-based Doppler radar and spaceborne, conventional radar returns.

1. Introduction

Recent general circulation model (GCM) studies have demonstrated the impact assumed fall velocities have on predictions of cloudiness and radiative forcing. Sensitivity studies using the European Centre for Medium-Range Weather Forecasts (ECMWF) model has been reported by Heymsfield and Iaquinta (2000) and Jakob (2002). These studies examined the relationship of global, radiative flux divergence to ensemble-mean ice crystal sedimentation rate, V_m. Relatively small changes in fall speed led to significant changes in the net global flux divergence. For V_m, using the expected range of 25 to 75 cm s^{-1}, the net flux varied over 8 W m^{-2}. Iacobellis et al. (2003) found in a 1D-column model that, as particle fall speed increases, the overall cloud fraction, cloud height, and grid-averaged ice water path decreased. The outgoing longwave radiation differed by up to 4 W m^{-2} over the range of fall speeds they examined. Given that 1 W m^{-2} converts roughly to

* The National Center for Atmospheric Research is sponsored by the National Science Foundation.

Corresponding author address: Andrew Heymsfield, National Center for Atmospheric Research, 3450 Mitchell Lane, Boulder, CO 80307.
E-mail: heyms1@ucar.edu

DOI: 10.1175/JAS3900.1

0.67 K in the earth's mean surface temperature, for climate models, reliable estimates of V_m are essential. In Part II of this study, in situ microphysical observations from Heymsfield et al. (2007, hereafter Part I) have been used with Doppler radar measurements to better constrain estimates of ice particle ensemble mass-dimensional relationships and mean, mass-weighted terminal velocities. In the past, these relationships have been difficult to constrain and evaluate.

Most GCMs now use some form of cloud microphysical parameterization to predict the mixing ratio of the condensate at a given time step and grid point, from a water mass continuity equation. For GCM models there are two ways to convert ice condensate to ice precipitation. One method uses a Kessler-type autoconversion scheme producing ice precipitation. The application of this scheme produces and removes condensate that can be converted to vapor or fall to the ground. Other GCMs allow precipitated ice to fall between cloud levels and to be retained from one time step to the next. Using the characteristics of the particle size distributions or relationships reported in the literature; that is, Heymsfield and Donner (1990), the rate of fall is determined by the IWC.

In GCM and weather forecast models, assumptions involved in the treatment of ice and snow fall speeds may lead to errors. As an example, the threshold for precipitation developed through autoconversion may be too large. As all of the particles in such a situation have zero fall velocity, they may only be removed through sublimation and, at low temperatures, sublimation rates are usually very low as well. Because of this effect, when compared with climatological data, these models may produce too-extensive areas of radiatively active cirrus cloud. Another source of error is applying mean sedimentation velocities to full size distributions. This too-quickly precipitates out smaller particles with lower fall speeds, resulting in too-small ice clouds. Another major source of uncertainty is the crystal concentration, or related particle size distribution (PSD) parameters such as the intercept concentration parameter N_0 (see Lin et al. 1983). Varying N_0 changes the mean particle size or slope of the PSD, and V_m. If accurate, mass-weighted fall speeds were available, this problem could be reduced by a double-moment approach in which particle numbers are moved by the number-weighted fall speeds and the masses by the mass-weighted ones.

Figure 1 shows the very wide range of V_m for a given IWC using both earlier and more recent parameterizations. Much of the spread is due to incomplete knowledge of ice cloud particle properties. For most parameterizations, a size distribution function is specified or

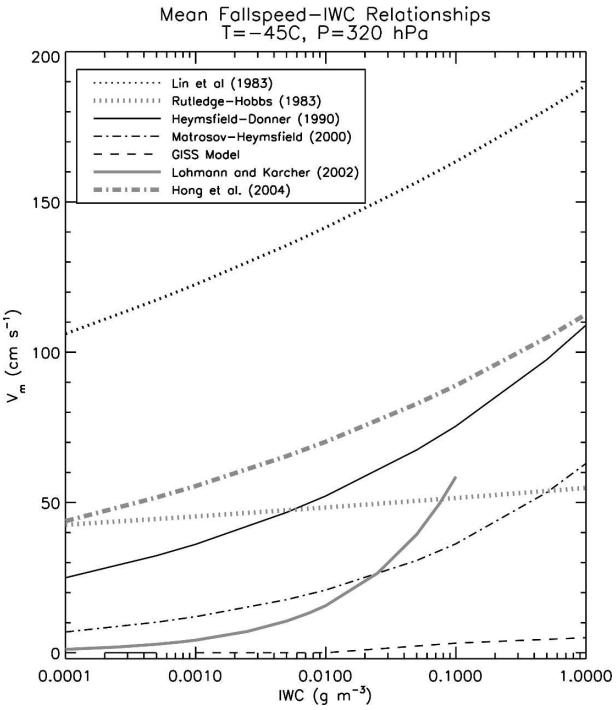

FIG. 1. Relationship between V_m and IWC from the investigators noted, from approximately the temperature and pressure levels shown. Curve for GISS model courtesy of A. DelGenio. Velocities for the ECHAM5 model (Lohmann and Kärcher 2002) assume pressure of 400 hPa, temperature of −40°C, and a number concentration of 0.1 cm^{-3} (U. Lohmann 2005, personal communication).

assumed. The V_m in most schemes is found analytically, from the size-dependent concentration, mass, and fall speed integrated from zero to infinity, divided by the ice water content. In these, an explicit fall velocity relationship, $V_t = AD^B$, and an adjustment for atmospheric pressure,[1] is used. Some representation of ice particle mass, m, in terms of ice particle maximum dimension, D, or a population-mean density, is required. Pressure or air density dependence is not specified explicitly in V_m parameterizations specific to cirrus, with relatively narrow ranges in pressure making such adjustments less necessary (Heymsfield and Donner 1990; Matrosov and Heymsfield 2000). The V_m–IWC relationships in these schemes are derived empirically, either from measurements of the PSD and estimates of particle masses and fall speeds, or from Doppler radar remote sensing of cirrus clouds. The lowest V_m values

[1] Although in Fig. 1 the chosen pressure of 320 hPa and temperature of −45°C are below those in some parameterizations, these conditions can occur in ice clouds formed in deep convection.

are in the Goddard Institute for Space Science (GISS) model and are intentionally so specified to correct for an upper troposphere model dry bias (A. DelGenio 2005, personal communication). The GISS parameterization also does not depend upon pressure. The Lin et al. (1983) one-moment microphysical scheme produces the largest V_m values, higher than Rutledge and Hobbs (1983) even though both methods use the same snow density (0.1 g cm^{-3}). This occurs because the two methods use different fall velocity relationships, adjusted slightly differently to account for the ambient atmospheric pressure.

As noted in Part I, an assumed distribution of particle mass with size might yield the correct IWC but not the correct V_m because they are differently weighted by the size distribution. This is illustrated by the curves in Fig. 2, which show the results of calculations of the reflectivity-weighted mean terminal velocity, V_Z. Here V_Z is approximately weighted by the square of the mass (section 2) instead of linearly by mass used in mean, mass-weighted ensemble fall speeds.

In Fig. 2, V_Z is plotted as a function of temperature for different values of the exponent b in the mass-dimensional relationship. The associated coefficient a, with PSD, produced IWCs yielding the measured value. Non-Rayleigh scattering effects, assuming spherical particles, are considered in these calculations (section 2), but are small at 8.6-mm radar wavelength. A method for refining the estimate of b is suggested by Fig. 2 because the assumed b produced a large range in V_Z.

Part I reports temperature-dependent coefficients for the mass-dimensional relationship. Here, in situ and Doppler radar remote sensing observations are used together to derive $m(D)$ relationships from which improved estimates of the lower and higher moments, including V_m, are derived. The methodology is briefly summarized in section 2 and the results of individual case studies are presented in section 3. Section 4 summarizes the principal findings of section 3. Section 5 evaluates representations of V_m used in earlier microphysical parameterizations in light of the new results. Section 6 develops parameterizations representing the results. The primary findings are summarized and conclusions drawn in section 7.

2. Methodology

This study uses in situ observations in middle- and low-latitude ice cloud layers sampled between −60° and 0°C. Five cloud layers referred to as synoptically generated were sampled at midlatitudes, four by the University of North Dakota (UND) Citation over the

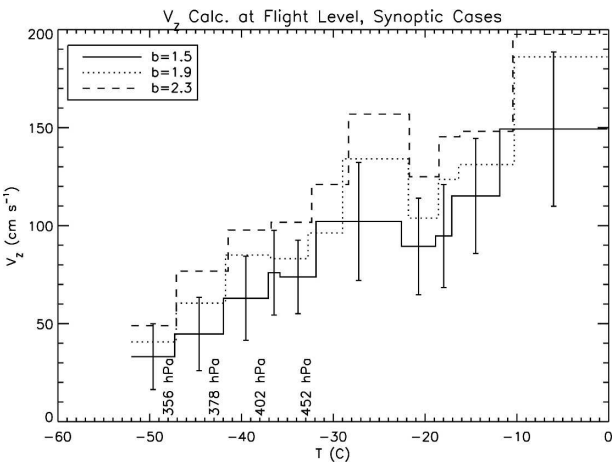

FIG. 2. For the synoptic cases reported in Part I, a relationship is found between the reflectivity-weighted mean fall speed, V_Z, calculated at a radar frequency of 35 GHz, and temperature for a range of exponents in the mass-dimensional relationship. For each data point, the coefficient is selected to reproduce the measured IWC from the particle size distribution. The error bars show the standard deviation of the points along the histogram for $b = 1.5$.

Department of Energy (DOE) Atmospheric Radiation Measurement (ARM) Southern Great Plains (SGP) site in the field program of the spring of 2000. The fifth case, in a deep-layer cloud with embedded convection, was sampled by the National Center for Atmospheric Research (NCAR) C130 during the Alliance Icing Research Study (AIRS-2) near Mirabel, Canada, on 19 November 2003 (Isaac et al. 2005). Ten flights, primarily in convectively generated, low-latitude ice cloud layers, were made by the UND Citation during the Cirrus Regional Study of Tropical Anvil and Cirrus Layers, of the Florida Area Cirrus Experiment (CRYSTAL FACE, hereinafter CF).

Size-spectra measurements and information on ice particle cross-sectional areas, for sizes from about 50 to 1000 μm, were obtained from Particle Measuring Systems (PMS) 2D-C probes, having resolutions of about 33 μm. For the ARM flights, a PMS 2D-P probe, sizing from 200 μm to more than 6 mm, was used. The CF and AIRS-2 programs used a Stratton Park Engineering Company (SPEC) high-volume precipitation spectrometer with a resolution of 200 μm to collect data from 200 μm to >1 cm. Particles objectively determined to have been shattered on the tips of the 2D probes were removed from the dataset (Field et al. 2006).

Relatively few particles are measured in the largest sizes of the imaging probes, thereby leading to statistical uncertainties in the measured PSD and calculated moments, especially the radar reflectivity, which is weighted by the largest but fewest particles. To evaluate the potential effects on Z_e, we specified statistical

errors in all size bins containing particles by assuming that the sample in each bin was Poisson distributed. Given that this statistical error is $1/\sqrt{N}$, where N is the number of particles per size bin per 5-s sample, we introduced an error of ± 1 standard deviation about N, altering the concentration in each bin appropriately. We used the mass-dimensional relationship of Brown and Francis (1995), with $b = 1.9$, for this evaluation. Applying this method to the 9 March (synoptic) and 26 July (CF, high IWC/reflectivity) cases resulted in mean changes in Z_e of $+3/-5$ dB and $+2/-3$ dB, respectively. Statistical uncertainties in the PSD from the imaging probes, therefore, will produce insignificant bias about the mean values.

A forward scattering spectrometer probe (FSSP) provided size distributions for particles from 2 to about 50 μm although, in those cases with large crystals, breakup in the probe's inlet may have led to overcounting (12 March, 19 November, and the CF clouds). Heymsfield et al. (2004, their Fig. A1 and associated text) show that in the IWC derived from the FSSP PSD for the CF clouds crystal breakup could produce an overestimate of the total IWC of about 5%. The effect on V_m would be even less.

FSSP and 2D particles were placed in one of the 48 size bins. Their average size distributions were measured over 5-s intervals, or about 0.75 km of horizontal flight. The cloud particle imager (CPI) probe collected high-resolution particle images. In the three field programs, a counterflow virtual impactor (CVI) directly measured the IWC.

Terminal velocity calculations require estimates of particle diameter, mass, cross-sectional area, drag coefficient, temperature (T), and pressure (P). Particle mass is expressed as a single, power-law relationship in the form

$$m = aD^b, \tag{1}$$

where D is the maximum imaged ice particle diameter. To span its likely range, in Part I, exponent b varied from 1.5 to 2.3. Using assumed values for b across this range, values for the coefficient, a, were determined by summing Eq. (1) across the entire binned size distribution and matching the measured IWC. This approach resulted in obvious errors. Below a given particle diameter, D_t, the mass of the particles exceeded that of solid ice spheres, thus implying that the particles were, in fact, solid spheres or drizzle. Using $b = 1.5$, however, 18% of the PSD from CF gave $D_t > 150$ μm, the percentage decreasing to 13% at $b = 1.7$ and to 12% at $b = 2.3$. The discussion and figures in the appendix in Part I suggest that many of these instances are due to overestimates of the measured IWC. When the IWC decreases rapidly, residual water is left in the CVI plumbing. Obviously anomalous points have been omitted from the dataset but some, difficult to remove objectively, still remain (Fig. A2; Part I). They have been implicitly removed by placing an upper limit on D_t.

Particle cross-sectional areas, A_c, were derived from 2D images. Each particle was assigned an area ratio, A_r, in which the particle area, A_c, was divided by the area of a sphere of the same maximum diameter. An average ratio, A_r, was found for the particles in each size bin. For particles in the FSSP size range, A_r was set to 1.0. Then, given A_c, D, T, and P, $V_t(D)$ was calculated using Mitchell and Heymsfield (2005).

In the preparation of Fig. 2 and later evaluations, radar reflectivity Z_e (mm^6 m^{-3}) was calculated using Mie scattering code (Bohren and Huffman 1983), assuming the particles to be spheres with the same D but with a density reduced to give the appropriate mass. This procedure is known to be of limited accuracy (Matrosov et al. 2005), because large ice particles are usually not spherical. For 95 GHz, Donovan et al. (2004) show that solid equivalent mass or equivalent area spheres compare well with discrete–dipole approximation (DDA) calculations for a range of idealized crystal shapes for $D < 1000$ μm. However, for larger values of D the accuracy of equivalent sphere formulations is very uncertain. Accordingly, in this work we emphasize results where our non-Rayleigh calculations indicate that non-Rayleigh effects are small. This applies in general to cold cirrus cases. For the warmer synoptic cases and the CF clouds non-Rayleigh scattering effects can be significant, sensitivity calculations indicating that there may be an uncertainty of up to 3 dB. Reflectivity-weighted fall speed, V_Z, was calculated as was V_m by summing the products of $Z_e(D_i)$ and $V_t(D_i)$ per particle size bin i, integrated over all bins, divided by the (total) Z_e.

For all five synoptic cases, Z_e and the Doppler fall speed, V_D, were derived from upwardly pointing Doppler radars. Here V_D is the sum of $V_Z + w$, where w is the air velocity. The millimeter-wavelength cloud radar (MMCR; 35-GHz frequency) is located at the SGP site in Oklahoma (36.61°N, 97.50°W). Dual frequency data is from the 33 and 95 GHz, University of Massachusetts' (UMass) collocated Doppler radars (Li et al. 2001). During the spring program in 2000, the radars, separated by a horizontal distance of 20 km, were located at the airport in Blackwell, Oklahoma (36.75°N, 97.35°W). In AIRS-2, in the fall of 2003, the McGill, X-band (9.4 GHz) Doppler radar operated at Mirabel, Canada (45.69°N, 74.03°W).

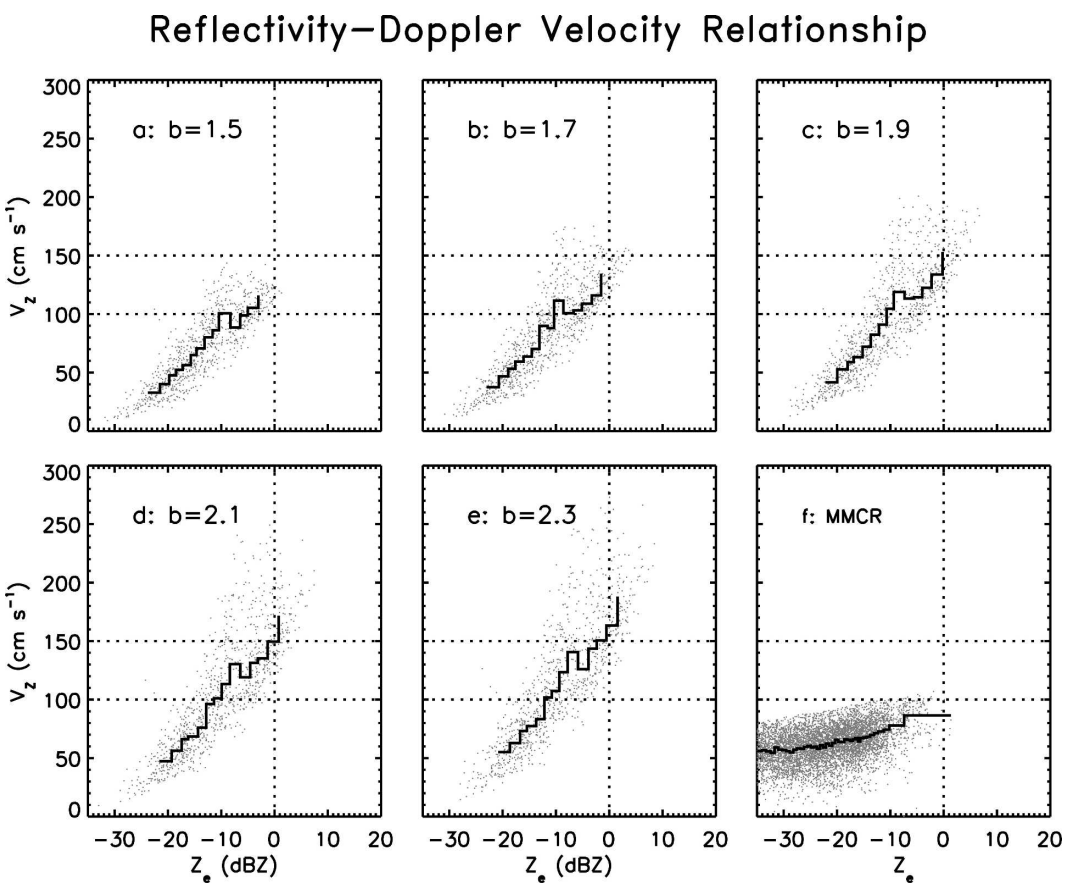

FIG. 3. (a)–(e) The relationship between Vz and dBZ for different values of the exponent, b, calculated with mass-specific points at a frequency of 35 GHz, and (f) measured by the MMCR radar. Stepped lines show median values, binned in (a)–(e) 15 and (f) 40 even increments of numbers of points. The time period is the same in all panels, 18.53 to 22.72 UTC hours (fractional hours are used for ease of plotting on a linear scale).

3. Results

This section reports the combination of a and b coefficients that may be used to accurately derive moments of the PSD: the second, IWC (approximate); the third divided by the second, V_m (approximate); the fourth, Z_e (approximate); and the fifth, divided by the fourth V_Z (approximate). Figure 2 shows that V_Z and Z_e are strong functions of the exponent b. The approach here is to compare the relationships of V_Z and Z_e from the Doppler radar data around the time of the in situ measurements, to those from the calculations using varying b. Rather than a 1:1 comparison of values obtained when the aircraft was within or close to the radar beam, this comparative approach has several advantages. It increases the sample size. It reduces the errors resulting from the large differences in sample volumes from aircraft probes and radar. It removes the uncertainties about the proximity of the aircraft to the radar and reduces possible errors in situ data noted in Part I.

a. 9 March 2000 ARM cirrus case

An extensively studied system of cirrus generating cells and trails on 9 March, was sampled in a Lagrangian-type spiral descent originating at cloud top and ending at cloud bottom. The UND Citation went from upwind to downwind of the ARM millimeter wavelength cloud radar (MMCR), passing over it in several loops of the spiral. The temperature ranged from −50° to −25°C and the pressure from 300 to 450 hPa. In this case, from below 100 μm to 500–1000 μm (Part I, their Fig. 2), the particles were almost exclusively bullet rosettes, and aggregates of bullet rosettes above that size range.

Figure 3 shows Z_e and V_Z calculated from the PSD at a radar wavelength of 35 GHz for the observed temperature and pressure and the MMCR measurements. In Fig. 3, the value of coefficient a for a given b was chosen to give the correct IWC. These comparisons do not raise questions about non-Rayleigh effects because calculated effects for this wavelength are <1 dBZ. The

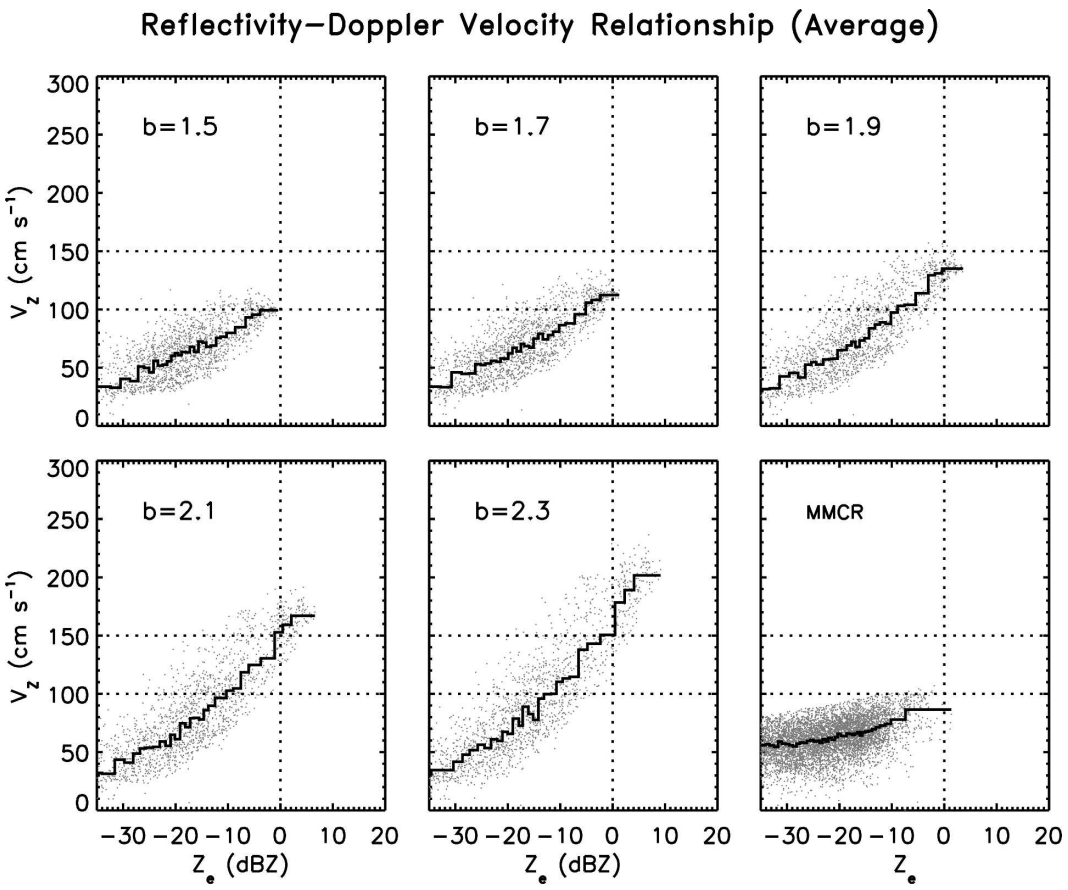

FIG. 4. As in Fig. 3 but using temperature-dependent, average values for the coefficient *a* from Part I.

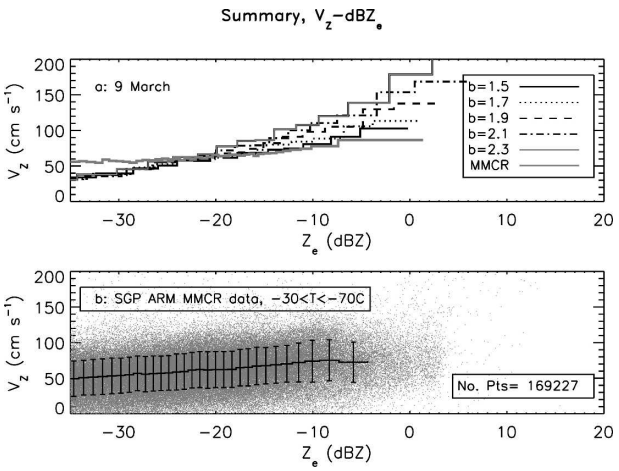

FIG. 5. Distribution of V_Z with Z_e: (a) measured and calculated from particle size distributions on 9 Mar 2000, using temperature-dependent average values for *a*; (b) summarized from SGP ARM MMCR data for November and December 1996, July 1997, and January and July 2000, in clouds in the −30° to −70°C range with optical depths of about 3–4 and below that are transmissible to the ARM ground-based lidar. Error bars are ± one standard deviation.

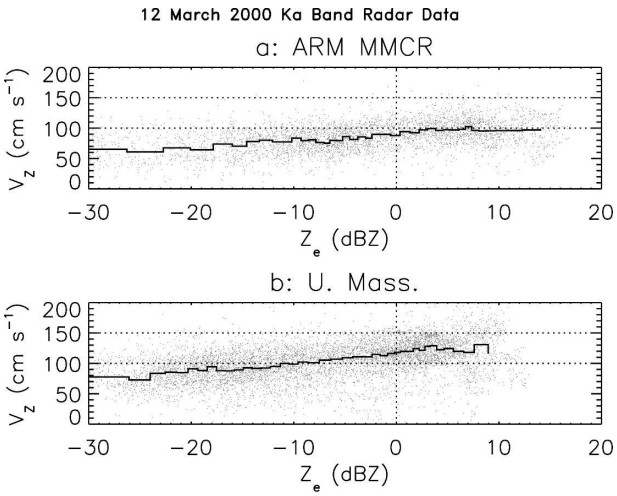

FIG. 6. 12 Mar 2000, vertically pointing, 35-GHz Doppler radar data, near the ARM SGP site from (a) the MMCR radar, from 22.75 to 25.73 UTC hours and (b) the UMass radar from 23.35 to 23.75 UTC hours. The MMCR data are from the Citation flight and the UMass data are from the stepped-down period of the flight.

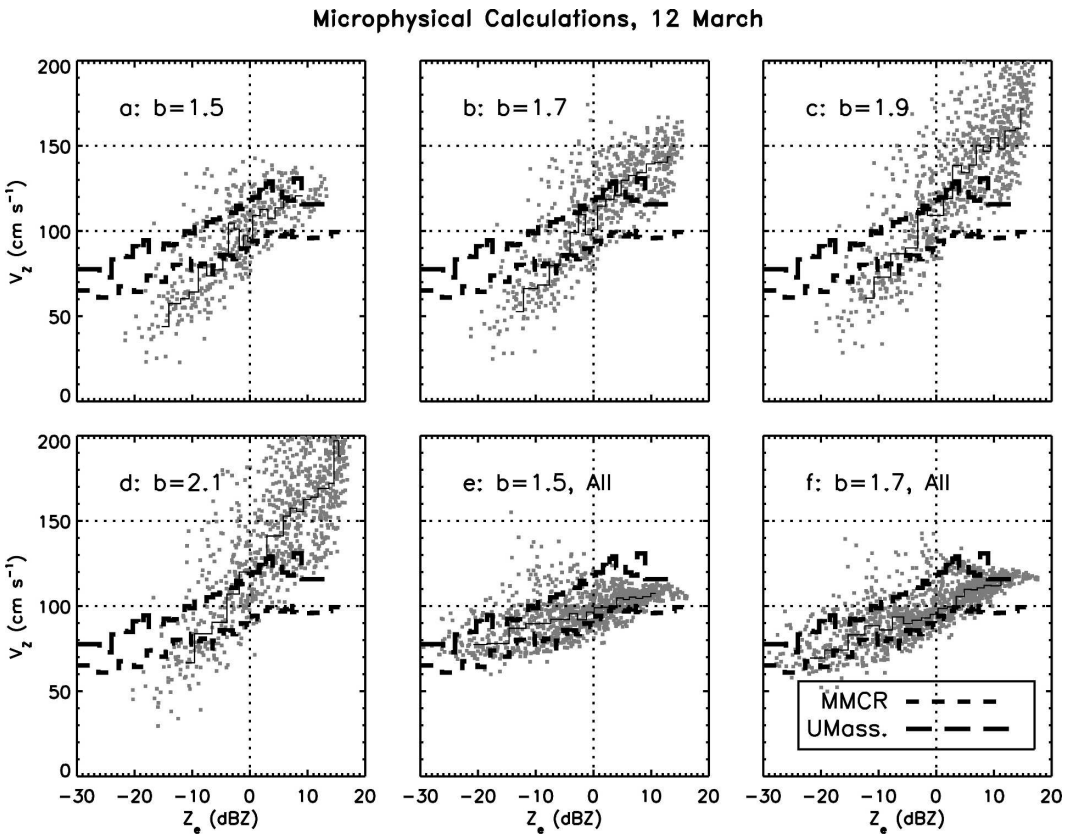

FIG. 7. (a)–(e) Calculations and (f) the MMCR radar measurements of Z_e and V_Z.

effect of air density on V_Z, which might amount to a decrease of 20% through the cloud layer, have been omitted in order to reduce the number of assumptions in the comparison. (It is implicitly considered in that low measured and calculated reflectivities tend to occur near the top of the layer and high ones near the bottom.) Note that in Fig. 3f, the measured Z_e is influenced by localized up- and downdrafts in the generating cells and trails. This results in a spread of the data about its mean: synoptic-scale uplift velocities will produce negligible effects. Figure 3 illustrates that, in the calculations and the observations, V_Z increases with Z_e. With increasing exponent b, the calculated V_Z and Z_e also increase (Figs. 3a–e). The best agreement with the measured peaks in Z_e and V_Z was $b = 1.5$ and 1.7.

Figure 3 does not include those times when the measured IWC was below the CVI detection threshold of 0.005–0.01 g m^{-3} or when rapid fluctuations in it produce hysteresis (Part I). On this day, in the spirals in and out of generating cells and trails, hysteresis was frequent and difficult to remove objectively. For all values of b, these effects contribute to the disagreement between calculated and measured values for $Z_e < -20$ dBZ.

A procedure has been developed to average the a coefficient as a function of temperature that mitigates the hysteresis effect and includes in-cloud points where the IWC < 0.005 g m^3. Average values for the coefficient a have been derived as a function of b and temperature, taken from Table 1 in Part I. Here, Figs. 4 and 5a show that using the average, temperature-dependent values for coefficient a improves the comparison between the range of Z_e and the slope of the distribution of Z_e with V_Z. This is especially true for the lowest values for b.

For reflectivities below -25 dBZ in Figs. 4 and 5a, there is a small, low bias in V_Z. For Z_e from -25 to -30 dBZ, the median diameter of the largest particles sampled is 345 μm, and from -30 to -35 dBZ, it is 285 μm. Particle areas derived from the 2D imaging probes are notoriously inaccurate for sizes below 200 or 250 μm, where relatively few imaging pixels are shadowed. This bias in V_Z where Z_e below -25 dBZ may be attributed to overestimates in the cross-sectional areas of the imaged particles in these cases, a conjecture borne out by Fig. 17 in Heymsfield and Miloshevich (2003), which compares cross-sectional areas measured by the 2D-C and higher resolution CPI probes. A 20% in-

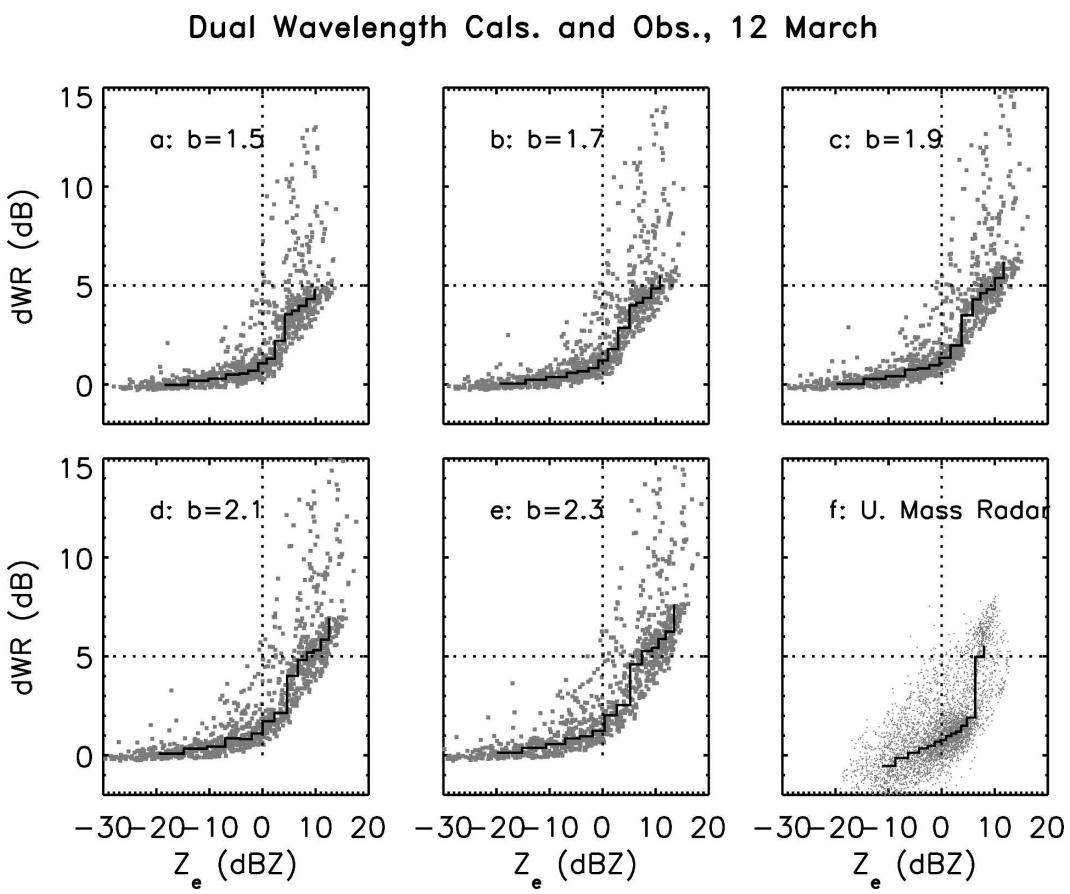

FIG. 8. Periods of Citation racetrack flights for 12 Mar 2000. Dual wavelength ratio calculations (dWR) from 22.78 to 24.72 UTC hours, and measurements as a function of Z_e, from two UMass radars, 35 and 94 GHz, from 23.35 to 23.73 UTC hours.

crease in the cross-sectional areas of sub-250-μm particles would correct much of the low bias.

The estimates of the exponent b for the case on 9 March may appear to be more generally applicable to cirrus clouds. The a coefficients are similar for all three cirrus cases (Part I) and bullet rosettes, typical in these cases, are the dominant crystal habit in synoptically generated cirrus (Lawson et al. 2006). This result is further illustrated in Fig. 5b showing ARM MMCR data for five months (see caption), from range gates where the temperature, derived from daily ARM SGP soundings, ranged from −30° to −70°C, the cloud optical depths were less than 3–4 (penetrable by lidar), and were nonprecipitating; with few exceptions, they are synoptically generated. Distribution of V_Z with Z_e and peak Z_e values agree closely with radar measurements on 9 March. The spread about the mean V_Z is probably due to up- and downdrafts that are additive or subtractive and may, in the mean, be slightly positive.

b. 12 March 2000 ARM ice cloud layer case

On this day, the UND Citation flew five racetrack patterns, each circuit passing over the SGP MMCR on the east and the 33 and 95 GHz, UMass radars on the west. Data from both radars are therefore available for this case. Each Citation track was conducted at progressively lower altitudes, warmer temperatures, and higher pressures, beginning near cloud top at 7.0 km, −30°C (450 HPa) and ending near cloud base at 4.2 km, −13°C (600 HPa) and from 23.06 to 24.72 UTC hours. The aircraft then centered on the MMCR radar, spiraling from below cloud base to above cloud top and from above the top to below the base, centered on the UMass radars. On this flight the particles sampled were visually more dense, with higher values for coefficient a than in the 9 March case (Part I, their Figs. 3 and 4). Though more dense, the particles were also bullet rosettes and other spatial crystals, with indications of crystal riming or of growth from riming sites. Because the

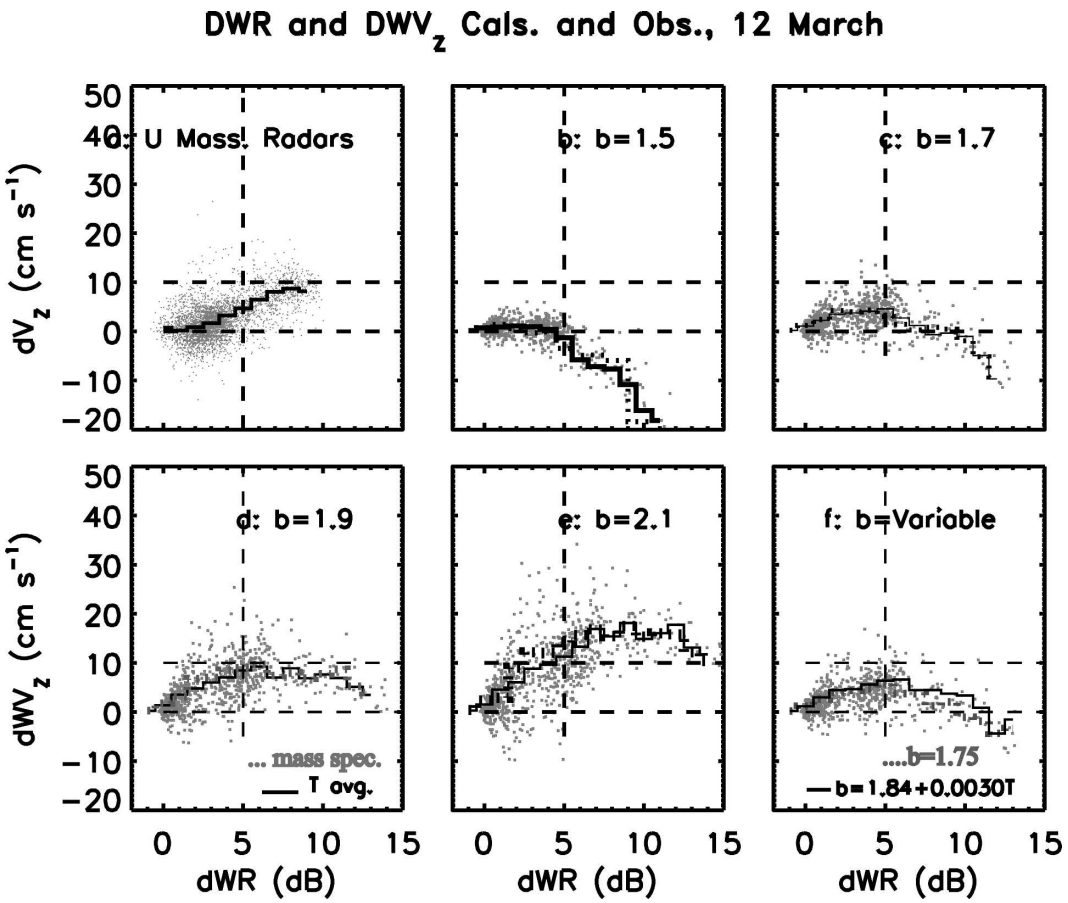

FIG. 9. Differential fall velocity and dWR at the UMass 33- and 95-GHz radar wavelengths for 12 Mar 2000. (a) Radar measurements and (b)–(f) calculations from airborne data.

precipitation probe was inoperable during the upward spiral and dissipating cloud was encountered on the downward spiral, the focus is on the periods of stepped descent.

As shown in Fig. 6, both the MMCR and the UMass 35-GHz Doppler fall speeds increase monotonically with Z_e, although the UMass radar is about 20–30 cm s^{-1} higher than MMCR. Given that the period encompassing the UMass data is much narrower than for the MMCR data, these differences can be expected. There may be vertical pointing errors in either of the radars that could also contribute to this difference.

Figures 7a–d show the V_Z–Z_e relationship for a range of values for b as derived from the measured IWC for the MMCR wavelength. Figures 7e,f show the results with b of 1.5 and 1.7 from the temperature-averaged values given in Part I. At this wavelength, non-Rayleigh effects were negligible and are not shown. In the figure, the calculations (points) and the measurements (dotted and dashed lines) compare favorably with $b = 1.7$.

Non-Rayleigh effects are sensitive to the wavelength

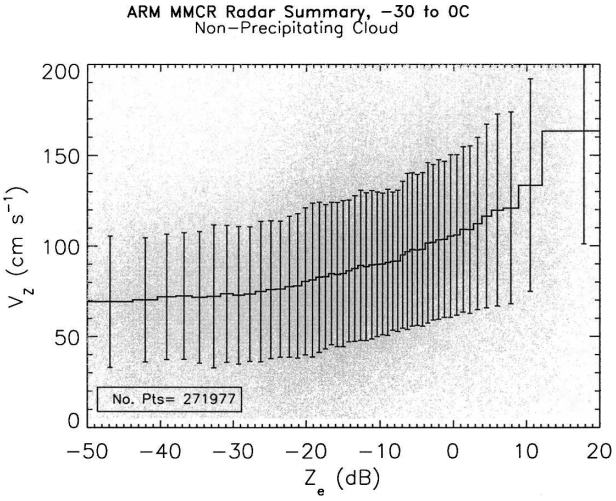

FIG. 10. ARM MMCR data from nonprecipitating ice cloud layers from 0° to −30°C, for the same periods as in Fig. 5b. Optical depths for most clouds are less than about 3–4.

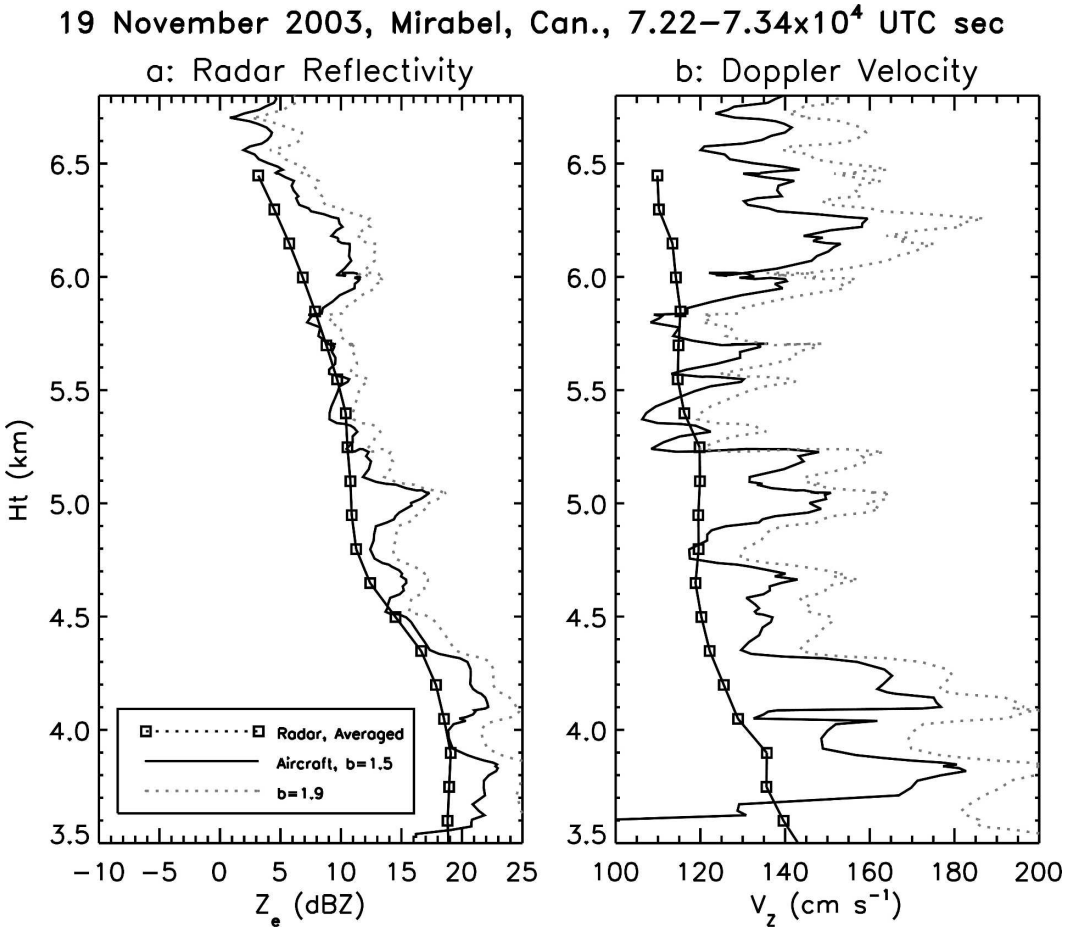

FIG. 11. Mirabel, Canada, airport, 19 Nov 2003, 20.06 to 20.34 UTC hours. (left) Comparison of calculated (from PSD) and measured reflectivities from the C130 and the McGill X-band (9.4 GHz) radar. The profiles follow the C130 altitude. Averaged profiles 10 min around the trajectory are used to simulate the effect of the 5–10-km radius of the spiral around the radar. To improve legibility, data have been smoothed over five points.

and mass of the largest particles that dominate the radar reflectivity (see Matrosov 1998). From the UMass radar, the dual wavelength ratio [dWR = dBZ_e (35 GHz) − dBZ_e (95 GHz)] was derived. The lowest dWR are for $b = 1.5$ and the highest ones are for $b = 2.3$. Although not shown, the dWR for each value of b increase with temperature, with the lowest values near −30°C and the highest ones near −10°C, close to cloud base; increasing particle size with temperature or depth of cloud below cloud top accounts for this result. The mean values of dWR derived from the PSD and Mie scattering calculations for $b = 1.7$ and 1.9 are within a few dB of those measured across the range of Z_e sampled (Fig. 8).

An examination of the differential fall speeds at the two UMass radar wavelengths, dWV_Z (Fig. 9), removes uncertainties arising from vertical air motions and for the most part antenna pointing angles. Figure 9a indi-

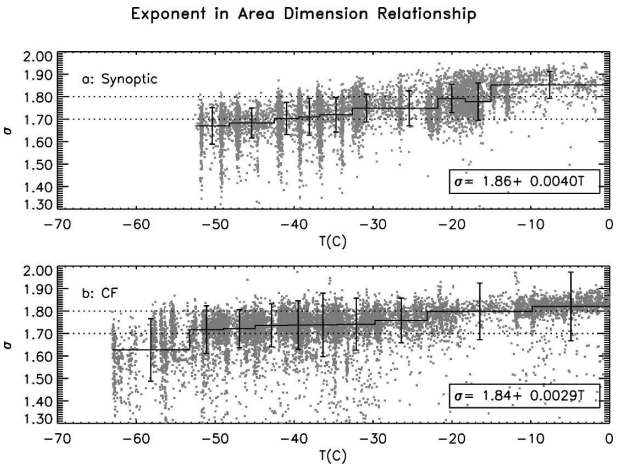

FIG. 12. Exponent in power-law area dimensional relationship, derived from curve fits to 2D imaging probe particle areas for each 5-s PSD; (a) synoptic, (b) CRYSTAL FACE.

TABLE 1. Temperature dependence of b, a (in $m = aD^b$) a(cgs) = $C_0 + C_1T$, temperature (T) in °C.

	b = 1.75	b = 1.86 + 0.0040 T (°C), synoptic b = 1.84 + 0.0029 T (°C), CF
Synoptic		
$<T$ (°C)	−37.0	−40.7
Min. a	0.000 60	0.000 49
C_0	0.003 811	0.003 909
C_1	6.70×10^{-5}	7.17×10^{-5}
$>T$ (°C)	−37.0	−40.7
C_0	0.002 757	0.003 258
C_1	3.85×10^{-5}	5.57×10^{-5}
CRYSTAL FACE		
$<T$ (°C)	−40.6	−39.6
Min. a	0.001 56	0.001 14
C_0	0.001 078	0.002 373 7
C_1	-7.61×10^{-6}	2.41×10^{-5}
$>T$ (°C)	−40.6	−39.6
C_0	0.004 408 6	0.004 955 8
C_1	7.03×10^{-5}	8.92×10^{-5}

TABLE 2. Temperature dependence of A, B in $V_t = AD^B$, P_0 = 1000 hPa A(cgs) = $C_0e^{C_1T}$, temperature (T) in °C, B (unitless) = $C_2 + C_3T$. For other levels, $V_t \propto [(\rho_0/\rho_a)]^{0.54}$, ρ_a is the air density at pressure level P.

	C_0	C_1	C_2	C_3
Synoptic				
b = 1.75	113	−0.0120	0.127	−0.0102
b = 1.86 + 0.004 T	131	−0.0138	0.185	−0.0084
CRYSTAL FACE				
b = 1.75	182	−0.0040	0.207	−0.0060
b = 1.84 + 0.0029 T (°C)	200	0.0004	0.244	−0.0049

cates that the measured dWV_Z increase roughly linearly with dWR over the range from 0 to 7 dB, at an average rate of about 1 cm s^{-1} dB^{-1}. For dWR from 7 to the peak value of 8 dB, dWV_Z is nearly constant. Peak dWV_Z values are about 12 cm s^{-1}. The calculated distribution of dWV_Z with dWR shows strong sensitivity to the choice of the b coefficient (Figs. 9b–e), al-

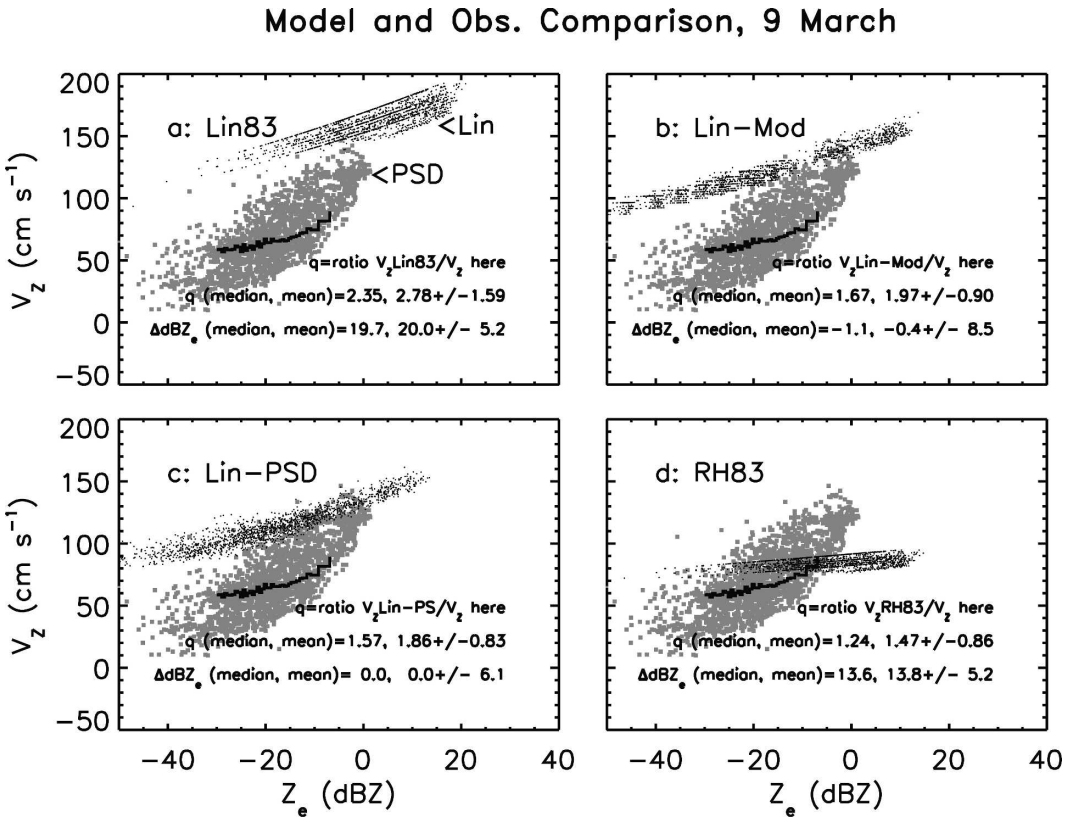

FIG. 13. 9 March cirrus case. Comparisons of earlier parameterizations with results from the present study. Each panel shows V_Z as a function of Z_e: small dots, calculations from one-moment schemes, light but larger dots calculated from the PSD with temperature-dependent, variable b, and stepwise histogram, Doppler radar data. (a) With Lin et al. (1983), and from PSD, each labeled, (b) as in (a), but numerically integrated over the size range from the particle probes, (c) as in (a) but using measured particle size distribution, and (d) using parameterization from RH83.

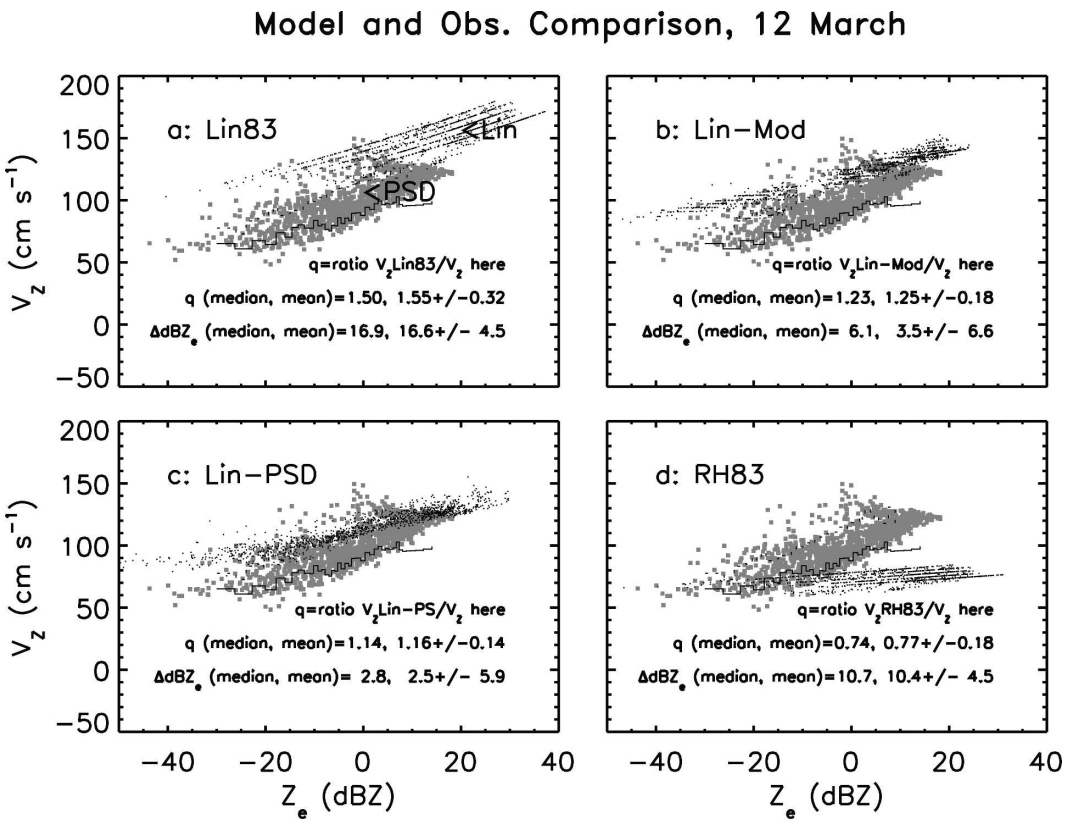

FIG. 14. Same as in Fig. 13, but for 12 March ARM case.

though there is virtually no difference found between using the mass-specific and temperature-averaged a coefficients (dotted and solid lines in the figure). For b of 1.5, there is a decrease in dWV_Z with dWR (Fig. 9b), whereas for b of 2.1 (Fig. 9e), the opposite is found. Although it is beyond the scope of this paper, we have fully accounted for the dWR–dV_Z relationship found in these estimates. The calculated trends are due to the progressive increase in particle size with increasing dWR (and air temperature) and a corresponding increase in particle cross-sectional area with temperature (discussed in section 4). These factors affect the distribution of particle fall speed with size, and V_Z, in the way shown.

Figure 9f shows two additional sets of calculations: one for $b = 1.75$ and a second for b that increases linearly from 1.75 to 1.84 between temperatures of −30° and 0°C. The rationale for a temperature-dependent b is discussed later in section 4. The curve representing the temperature-varying b produces an excellent match with the observations for dWR between 0 and 6 dB, where most of the measurements are obtained. A certain caution should be noted, however, that the dWV_Z values are extremely small. A slight difference in the two wavelength radar characteristics or radar antenna–pointing angles could lead to errors in interpretation. Uncertainties in accounting for non-Rayleigh scattering at 95 GHz may also impact the interpretation.

On 12 March, the sampled cloud is likely to be quite typical of nonprecipitating, ice cloud layers in the temperature range from 0° to −30°C. Figure 10 shows the relationship between dBZ and V_Z in nonprecipitating, lidar-transmissive, ice cloud layers between 0° and −30°C, scanned by the ARM MMCR, showing strong commonality with the 12 March observations.

c. 19 November 2003 AIRS-2 case

On 19 November 2003, a deep cloud layer extended over the McGill University radar site at Mirabel Airport, Canada. The radar detected a continuous bright band at about 2.8 km and embedded convection extending from the bright band to about 4 km, with a cloud top at about 7 km. The NCAR C130 conducted five Eulerian ascents and descents through the cloud layer from 17.50 to 21.67 UTC hours. The diameter of the spirals was about 14 km, centered on the radar. For all but the fourth spiral, liquid water contents measured by a King probe and exceeding 0.1 g m^{-3}, were found to extend several degrees below 0°C. During some of the

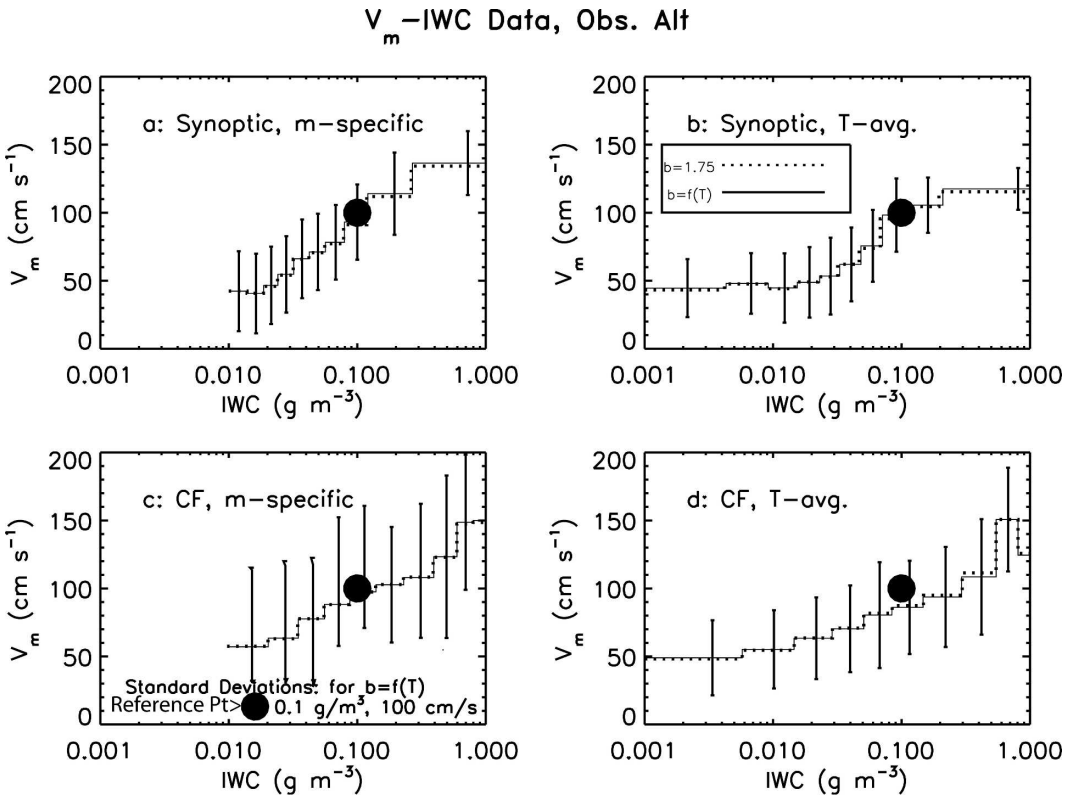

FIG. 15. Mass-weighted mean fall speed at aircraft pressure level versus IWC for b of 1.75 and as a function of temperature, for (a) synoptic case, constrained by measured IWC; (b) as in (a) but using mass parameterization; (c),(d) as in (a) and (b), but for CRYSTAL-FACE cases. Solid circles denote reference point.

spirals, LWC was intermittently detected at temperatures as low as −20°C. In this instance, the collocated radar and aircraft data are sufficiently resolved in time and height to facilitate direct comparison of the Doppler measurements and the calculations.

Data from the fourth aircraft spiral has been used to evaluate calculations where the reflectivities are in the range 15 to 25 dBZ, and the King probe data showed no liquid water content greater than 0.05 g m^{-3}. At the McGill radar frequency of 9.4-GHz, non-Rayleigh scattering effects are minimal. Because the CPI images showed liquid or recently frozen droplets 20 to 30 μm and as high as 3.5 km or −3.5°C, the comparisons were limited to the flight above that height. The predominant crystals were needles, single and aggregates, some rimed, and dendritic and aggregates of dendritic crystals. As is shown in Fig. 11a, the calculated reflectivities compared very well with the measurements, with little difference between exponent b having been 1.5 or 1.9. The resultant Z_e was comparable for the calculations for b of 1.5 and 1.9, leaving the choice of a value for exponent b from the calculations unanswered. In Fig. 11b, V_Z compared reasonably well with the measurements, especially so because vertical motions in the cloud layer were detected by the radar and the aircraft. The resulting V_Z, with b of 1.5, were approximately 20 cm s^{-1} lower and agreed better with the measurements than with b of 1.9.

4. Interpretation of radar–aircraft intercomparison

From section 3, the magnitudes of Z_e ($=10^{\mathrm{dBZ}/10}$) and V_Z, and their relationship, are a strong function of the exponent b. The aircraft–radar data from 9 March (Figs. 4 and 5a) suggest that b is close to 1.5, but a range of 1.5 to 1.7 is more likely. This is because net updrafts may have produced the cirrus that would have reduced the measured V_Z. We also conclude from the synthesized Doppler radar observations from −30° to −70°C (Fig. 5b) that below −30°C, b is between 1.5 and 1.7. The dWR–dV_Z relationship measured on 12 March and calculated using b = 1.7 and 1.9 (Figs. 9a,c,d) suggests that between −30° and 0°C, b is about 1.75 or 1.8. As shown in Fig. 9f, the calculations using a b that increases linearly with temperature fit the observations quite closely. The MMCR radar observations from −30° to 0°C (Figs. 6 and 10), and for the AIRS-2 case (Fig. 11) are consistent with b = 1.7 to 1.9. In CF clouds

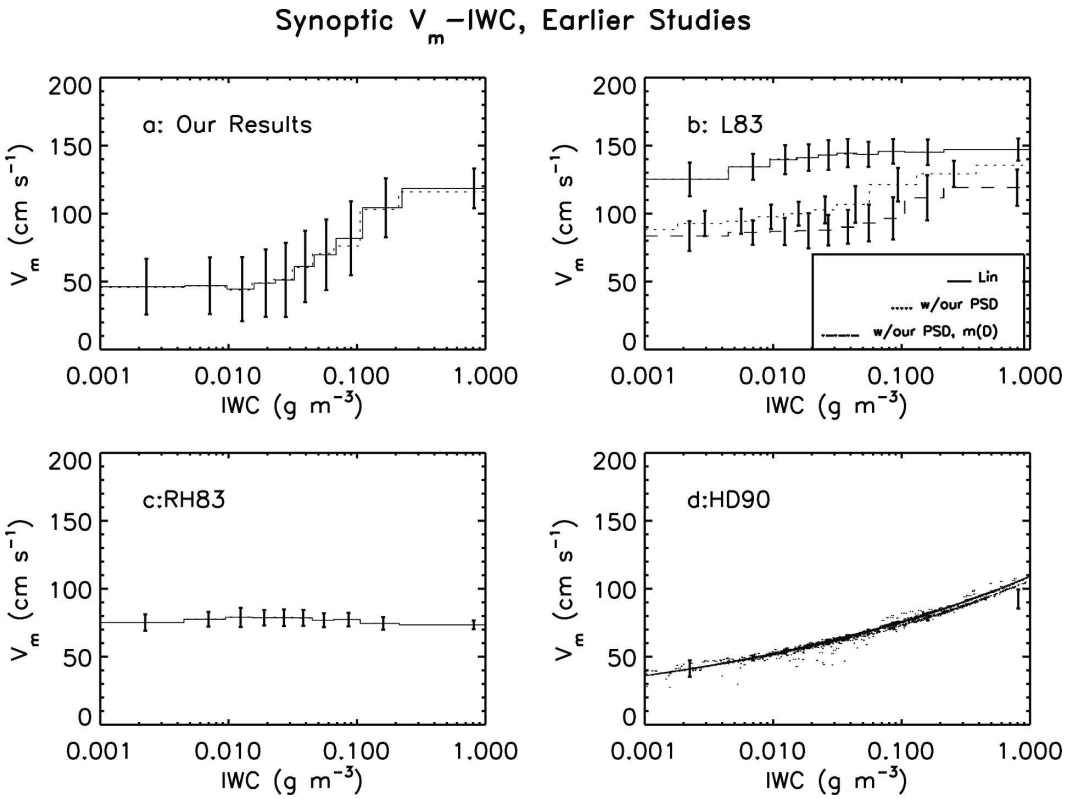

FIG. 16. Comparison of the parameterizations of mass-weighted fall velocity as a function of IWC. (a) Present results for b, 1.5 to 2.1, temperature-dependent mass coefficients. (b) Lin et al. (1983) with modifications as described in the text, (c) Rutledge and Hobbs (1984), (d) Heymsfield and Donner (1990).

between −25° and −52°C, Heymsfield et al. (2005) have shown that b of 1.6 fits coincident radar/aircraft observations.

The results cited above are consistent with observation and theory in fractal mass aggregates in several systems (e.g., colloidal particles in the presence of electrolytes). Although the rosettes dominating the colder temperature observations are not strictly aggregates, rosette aggregates have been observed. In mass fractal aggregates, if b is less than 2, the b exponent is preserved in the projection to cross-sectional area (σ), where σ is the exponent in the area dimensional relationship, a condition known as geometric transparency (Bushell et al. 2002). Because b is evidently less than 2, if the particles are aggregates, b and σ should have the same value. Figure 12 indicates strong dependence on temperature in σ derived from power-law fitted to the 2D particle image areas. The particles are from 5-s PSD given in Part I and the dependence is consistent with inferences drawn from section 3 herein. At warmer temperatures where aggregation dominates, σ tends to 2.0, consistent with the results reported by Westbrook et al. (2004). There is little difference between tendencies in synoptic and CF datasets. If a and b have the same values, an average of 1.75 for b, or one that increases with temperature, would fit the observations well. Table 1 gives curves representing the temperature dependence of a for b of 1.75 and with b varying with temperature. The a coefficients have been derived using the CVI IWC, as in Part I. The corresponding terminal velocity coefficients A and B in the relationship $V_t = AD^B$, normalized for a pressure level of 1000 hPa, are shown in Table 2. The a and b coefficients are valid for the full range of particle sizes and the A and B are valid for particles 100 μm and above, as in Part I.

5. Evaluation of earlier microphysical model parameterizations

The coincident, in situ, and radar observations given in section 3, present an unique opportunity to evaluate microphysical parameterizations of ensemble mean particle velocities for snow used in the earlier studies, specifically aspects of Lin et al. (1983, hereafter L83) and Rutledge and Hobbs (1983, hereafter RH83). Particularly interesting for evaluation in the two studies are the fall velocity relationships in Locatelli and Hobbs (1974), from which the fall velocities in the parameter-

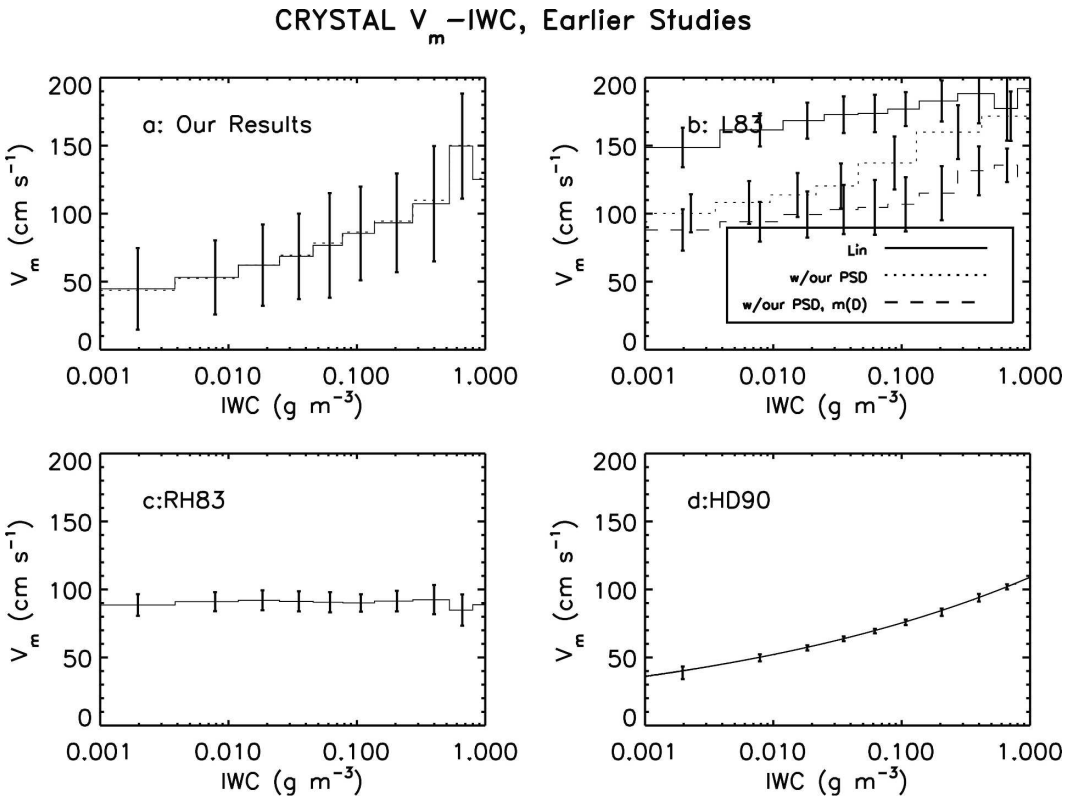

FIG. 17. As in Fig. 6, for CRYSTAL FACE ice clouds: except (a) where mass-specific coefficients are used.

izations are based on. We may also compare our results with those reported for cirrus by Heymsfield and Donner (1990, hereafter HD90). Errors in microphysical assumptions are amplified more by the Z_e and V_Z terms than they are by IWC or V_m. Now there are radar and in situ datasets that one can use to test the model calculations. We look first at how these earlier parameterizations predict the actual radar measurements. With a better understanding, it is then possible to evaluate errors in the V_m parameters.

The basic variables in L83 and RH83 are the slope of the exponential PSD, λ, the PSD intercept N_0, the assumed ice density ρ_i, the fall speed relationship $V_t = AD^B$, and the adjustments for air density. L83 takes $N_0 = 0.03$ cm^{-4} and RH83 as 0.2 cm^{-4}. The λ is derived analytically from the IWC, ρ_i, and N_0. By integrating these variables to represent Z_e and V_Z, analytical relationships are developed between them. [The derivation of V_Z and Z_e for an exponential PSD is given by Heymsfield et al. (2002) and others. Non-Rayleigh scattering is not included.] The V_Z for the L83 and RH83 schemes are a function of A, B, λ, and indirectly ρ_i through the effect on λ whereas Z_e depends on ρ_i, N_0, and λ.

The values of the PSD parameters in L83 and RH83 were not derived for cirrus clouds but it is interesting to evaluate their applicability in such conditions, especially where non-Rayleigh effects are negligible. The comparisons are given in Fig. 13 where the measured and calculated (for temperature-dependent b from Fig. 12) distributions of V_Z to Z_e in the 9 March ARM case are compared with earlier calculations. The differences in the results from L83 are particularly noticeable.

In Fig. 13b λ and N_0 values from L83 have been used to produce PSD by numerical integration over the size range measured by our particle probes instead of integrating the function from 0 to infinity, which improved the results. In Fig. 13c, V_Z and Z_e are estimated from the PSD from the particle probes and the ρ_i, A, and B from L83, which improved the agreement with radar data. In Fig. 13d, the RH83 coefficients with a higher N_0 and lower terminal velocities than L83 have been used. Here V_Z is within several tens of cm s^{-1} of the observations but Z_e is close to those of L83 and are as much as 15 dB higher than observed. The V_Z relationship is, therefore, appropriate but the ice densities too high.

Figure 14 shows the same plots as in Fig. 13, except for the warmer 12 March case. Similar results are noted: an ice density of 0.1 g m^{-3} is too large for the larger

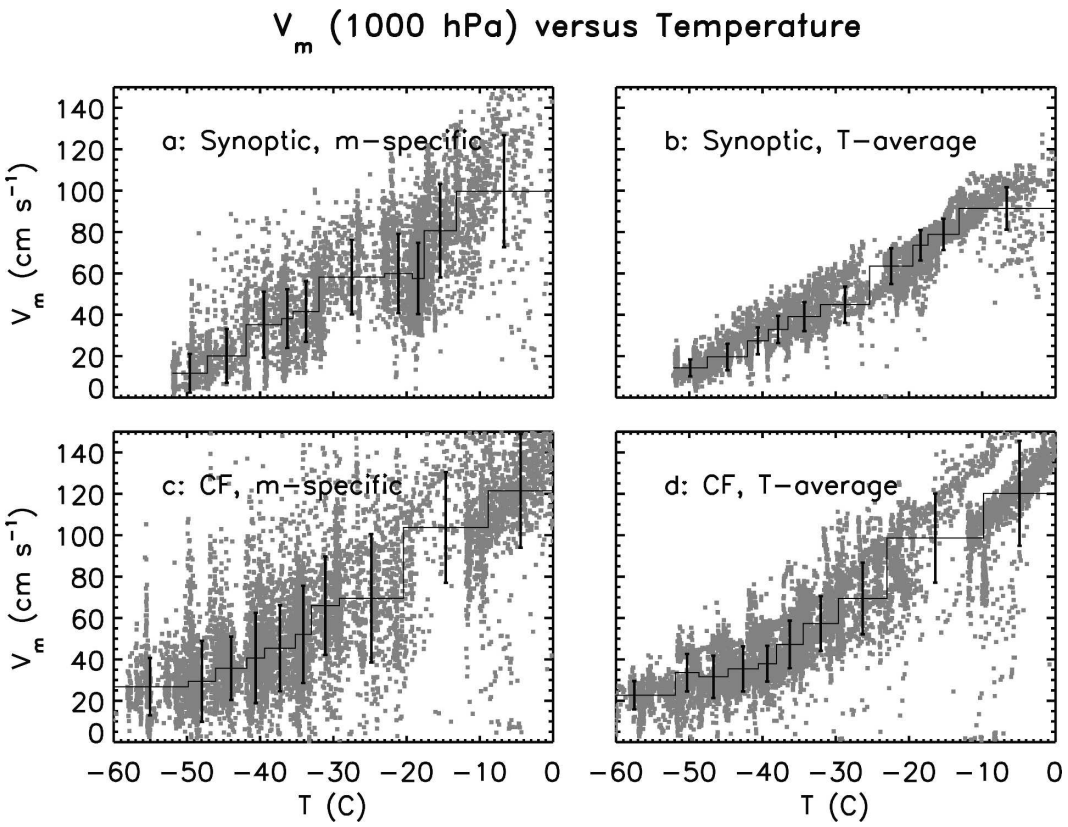

FIG. 18. (a), (b) V_m as a function of temperature. (c) Synoptic cases, CRYSTAL FACE, mass-specific a coefficient with $b = 1.75$; (d) as in (c) with temperature-dependent b and associated temperature-averaged a.

particles because the Z_e are overpredicted; the V_Z from L83 overpredict the observations and those from RH83 are flat and likely underpredict the observations; and, improvements are gained by using the measured rather than parameterized PSD.

Our goal is to derive accurate V_m over a wide range of IWC for synoptically and convectively generated ice cloud layers and to ascertain factors that lead to errors in earlier derivations. In Fig. 15, our V_m increase IWC, as expected from the results shown in Fig. 1. The mass parameterizations provide results that are comparable to those that use the IWC to constrain the mass estimates (cf. Fig. 15b to Fig. 15a and Fig. 15d to Fig. 15c) and have the advantage that they extend to lower IWC. The higher masses associated with the CF cases yield higher V_m than for the synoptic cases.

The relationship between V_m and IWC from Figs. 15b,d is replotted in Fig. 16a for synoptic cases and in Fig. 17a for CF cases. They are used as references because they extend to IWCs below those measured by the CVI. Figures 16b and 17b show V_m as a function of IWC using 1) the L83 approach, 2) L83 ice densities and fall velocities with the measured PSD, and 3) the measured PSD for exponent b of 1.7 with temperature-dependent particle masses as in Figs. 16a and 17a. With 3), the calculations represent a significant improvement but the mismatch with the results in Figs. 16a and 17a indicate that for small particles or low IWCs V_t from Locatelli and Hobbs (1974) is overpredicted. In Figs. 16c and 17c, V_m from RH83 is unrealistic, showing only slight dependence on IWC. This is probably explained by the use of an unrealistic V_t–D relationship. Other variables in RH83, particularly ice density, are similar to L83. From Figs. 16d and 17d, for the range for which it was developed, the HD90 expression produces good results for IWC < 0.1 g m^{-3}. In Fig. 16d, note the scatter in V_m (dashed curve). The HD90 relationship should produce a monotonic curve. The V_m was calculated using $b = 1.5$, but the IWC, derived from temperature-dependent mass coefficients for all values of b, varies only slightly. In this figure, therefore, the spread represents the spread in IWC and it is remarkable that it is so small. This is due in part to the V_m dependence on IWC, developed in HD90.

6. Parameterizations

Based on the results given in section 5, the temperature and IWC dependencies of V_m are parameterized

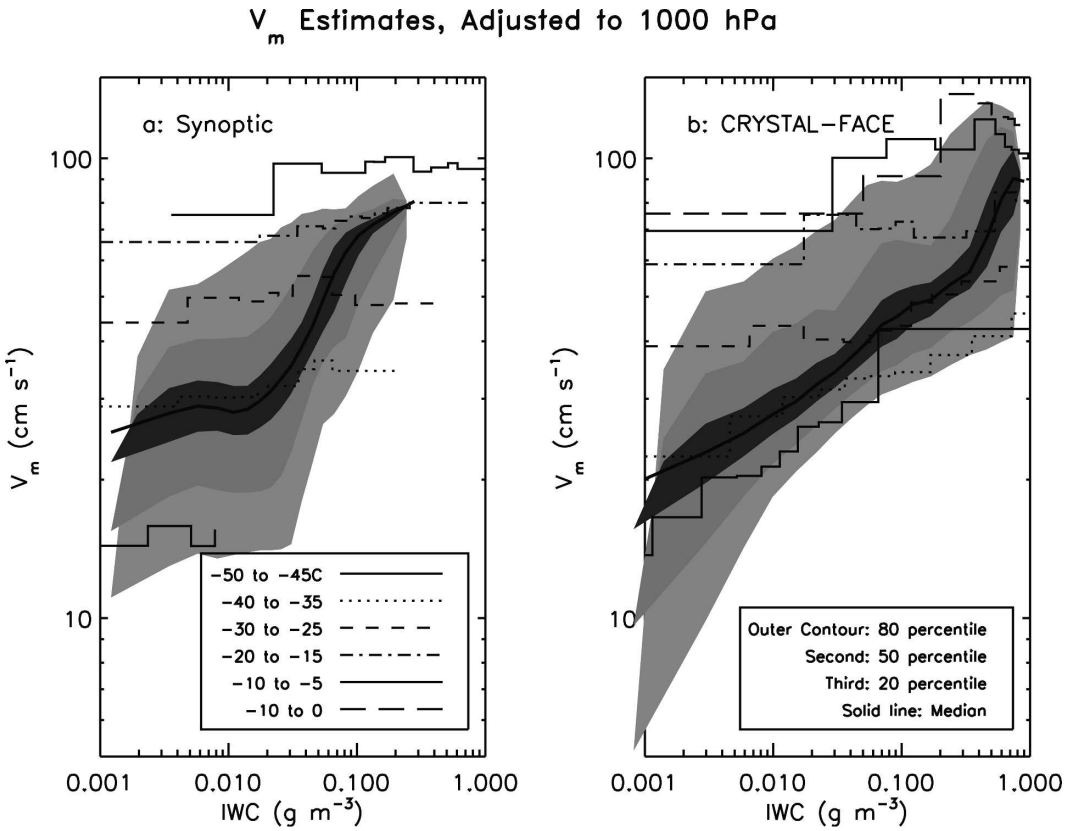

FIG. 19. Mean, mass-weighted fall speeds as a (a) function of IWC; (b) synoptic cases; CRYSTAL FACE cases, using temperature-dependent coefficient a and temperature-dependent exponent b. Contours enclose various percentiles of the data points. Lines give median values for certain temperature ranges.

from the temperature. Two sets of calculations from the results presented in section 4 are examined: one using $b = 1.75$ and a obtained directly from the IWC (mass specific), and the second using temperature-dependent b and the associated, temperature-averaged a. To generalize the results, the pressure and temperature of the observations have been adjusted to surface (air density) conditions P_0 of 1000 hPa and 0°C according to $[\rho_0/\rho(T, P)]^{0.54}$ from Part I. Figure 18 shows a strong dependence of V_m on temperature for the synoptic (Figs. 18a,b) and CF (Figs. 18c,d) datasets. In the figure, the primary difference between the mass-specific and the temperature-averaged coefficients is that the latter, because of the averaging, have a much reduced scatter. At temperatures close to 0°C, the synoptic and the CF datasets are about the same but, at lower temperatures, the CF values are much larger. Given that convective mixing produces more homogeneous particle properties throughout the cloud column, this is not surprising.

In each Fig. 18 panel, and also as noted in Fig. 15, much of the scatter about the means may be attributed to variability in IWC. The trend is further investigated in Fig. 19, specifically for variable b and temperature-averaged a. The contours in this figure are probability distributions enclosing [IWC, V_m] points where the features noted in Fig. 15 exist. In Figs. 19a,b, the nearly horizontal lines show the median values for V_m as a function of IWC, partitioned according to temperature. With a given IWC, V_m increases with temperature, reflecting the broadening of the PSD to larger sizes as the temperature increases.

The median value for V_m as a function of IWC for all of the data combined (dark, solid line in Fig. 19) clearly does not account for the V_m dependence on temperature, and cannot be a curve universally applicable to ice clouds with wide temperature ranges. The IWC–V_m dependence, accounting for temperature has been fitted to the data in Fig. 19 as

$$V_m[\text{cm s}^{-1}] = (a_0 + a_1 T[^\circ\text{C}])\text{IWC}^{(b_0 + b_1 T)}, \qquad (2)$$

where for the synoptic (CF) cases $a_0 = 120.4$, $a_1 = 2.21$, $b_0 = 0.0487$, $b_1 = 4.57 \times 10^{-4}$ ($a_0 = 135.3$, $a_1 = 1.93$, $b_0 = 0.0058$, $b_1 = -0.002\,453\,9$), and the median ratio

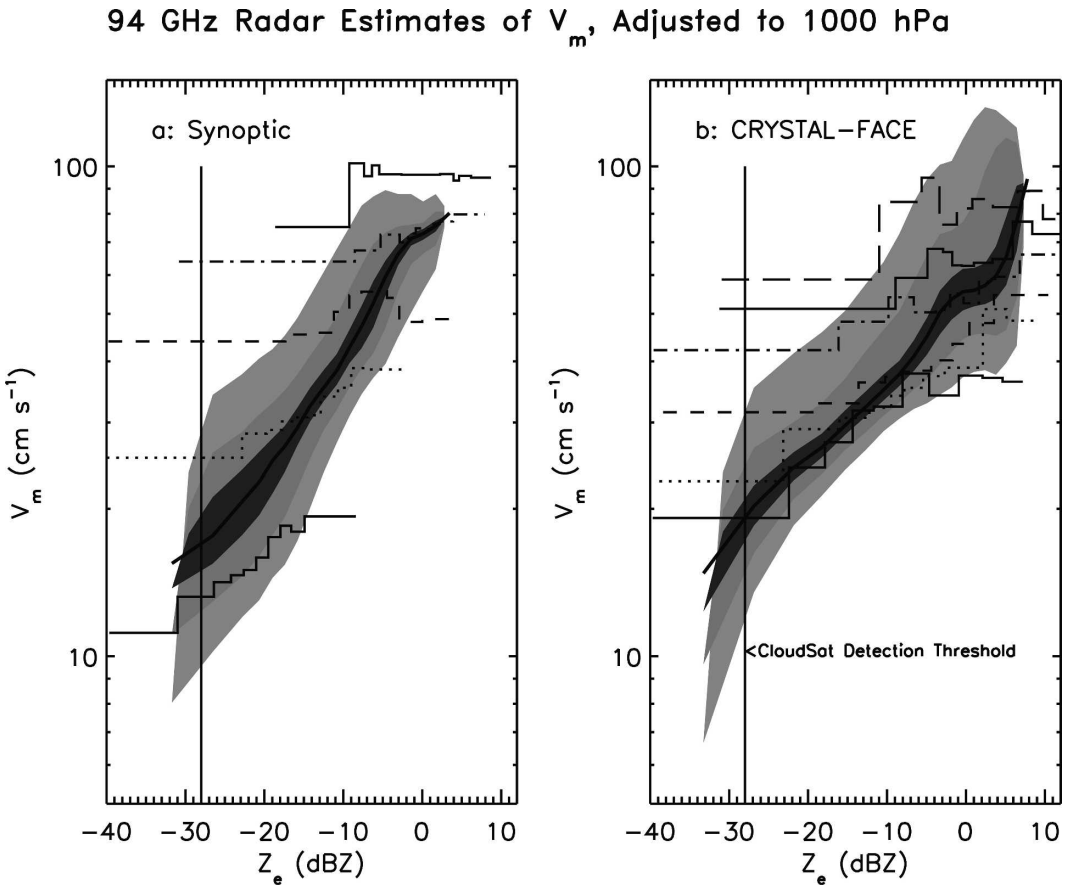

FIG. 20. Same as Fig. 19, but with the equivalent radar reflectivity derived for a radar frequency of 94 GHz as the abscissa.

of the predicted to derived V_m is 0.99 (1.09), with 75% (65%) of the points falling within 20% of the mean.

The combination of spaceborne and ground-based radars presents an opportunity to derive vertical profiles of the fall velocity of cloud ice particle ensembles on a global basis. Figure 20 shows the temperature dependence of the relationship of V_m (temperature-varying b) to Z_e, at the frequency of the CloudSat radar, 95 GHz. The results in this figure are fitted by the relationship

$$V_m[\text{cm s}^{-1}] = c_0 + c_1 T[^\circ\text{C}] + Z_e[\text{dB}Z \text{ at } 94 \text{ GHz}]^{(d_0 + d_1 T)}, \quad (3)$$

where for the synoptic (CF) cases $c_0 = 109.3$, $c_1 = 1.87$, $d_0 = 0.782$, $d_1 = 0.00944$ ($c_0 = 82.4$, $c_1 = 0.92$, $c_0 = 0.8117$, $c_1 = 0.004\,087$), and the median ratio of the predicted to derived V_m is 0.99 (0.92). The approximate temperature may be derived from the CloudSat data stream. Synoptic and convective ice clouds may be differentiated on the basis of height- (or temperature-) dependence of Z_e. In Fig. 20, we estimate the uncertainty for $Z_e < 20$ dBZ to be 3 dBZ or less, if we consider aggregates to be oblate with their long axes horizontal and use the T-matrix scattering calculations of Matrosov et al. (2005). In Fig. 20, scatter in V_m is much less than in Fig. 19, probably from the variability in the particle cross-sectional area in the V_t calculations.

A ground-based Doppler radar operating in a vertically pointing mode can provide more accurate estimates for V_m. Orr and Kropfli (1999) removed vertical motions by averaging over 10-min time scales and quite accurate Vz were then obtained. Figure 21 shows the relationship of V_m/V_z to Z_e at a frequency of 35 GHz. These calculations are derived from the PSD for a temperature-varying b but the ratio is relatively independent of b. The following expresses the temperature dependence of the ratio

$$\frac{V_m}{Vz} = w_0 + w_1 T[^\circ\text{C}] + Z_e[\text{dB}Z \text{ at } 35 \text{ GHz}]^{(x_0 + x_1 T)}, \quad (4)$$

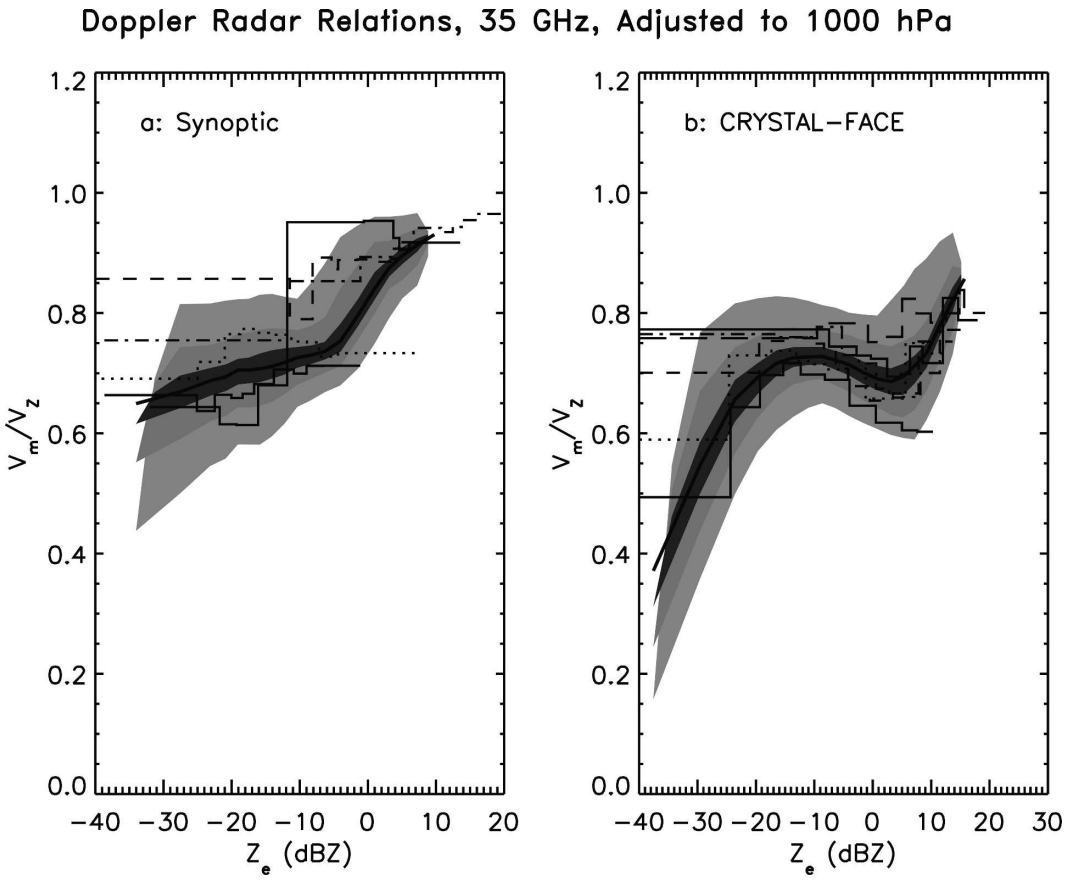

FIG. 21. Same as Fig. 19, with equivalent reflectivity derived for 35 GHz as the abscissa and the ratio of the mass to reflectivity-weighted fall speeds at 35 GHz as the ordinate.

where the ratio should be limited to a maximum of 0.95. For the synoptic (CF) cases $w_0 = 0.94$, $w_1 = 0.0044$, $x_0 = 0.00935$, $x_1 = 0.00019$ ($w_0 = 0.78$, $w_1 = 0.00210$, $x_0 = -0.00157$, $x_1 = -5.082 \times 10^{-5}$, and the median ratio of the predicted to derived V_m is 1.02 (0.96).

These results suggest that long term estimates of V_m from ARM Doppler radars at several locations and non-ARM sites, like the three CloudNET European sites, could be used to evaluate spaceborne radar data.

7. Summary and conclusions

Part II of this study includes synthesized particle size distributions, direct measurements of ice water content, and vertically pointing Doppler radar measurements. The results produce coefficients in mass-dimensional relationships yielding accurate estimates of lower and higher moments from particle size distributions including ice water content, mean, mass- and reflectivity-related fall speeds, and radar reflectivity. We have also used the results to evaluate earlier bulk-parameterization methods relating ice water content to the mean, mass-weighted fall speed. The methods have been improved by incorporating better estimates of size and pressure-dependent fall speeds. Parameterizations of mass-weighted ensemble fall speeds as a function of the ice water content have also been improved by incorporating temperature dependence. Parameterizations have been developed to derive V_m from a 95-GHz spaceborne radar, and to evaluate these products using ground-based, vertically pointing Doppler radars.

It has been found that earlier, one-moment, bulk parameterizations, developed for cloud modeling studies, rely upon fall speed relationships that produce significant error. Such parameterizations may be reformulated to include temperature-dependent mass coefficients, a and b, (in $m = aD^b$) and A and B (in $V_t = AD^B$), from Tables 1 and 2. To account for varying atmospheric pressure (air density), adjustments in V_t can also be improved (Part I). Inclusion of a temperature-dependent, particle size distribution slope parameter, into a one-moment parameterization could reduce the need to assume a constant value for the intercept parameter of the PSD, N_0. These improvements could

also be included in two-moment parameterization schemes and for bin-resolved models as well. Fall velocity relationships can be incorporated into two-moment microphysical schemes such as that advanced by Field et al. (2005) and others.

The testing methods advanced in this report should be part of the evaluation of bulk microphysical schemes. In so far as a consistent set of the variables, IWC, V_m, V_Z, and Z_e is obtained at multiple wavelengths, modeling case studies may be compared with coincident, or long-term, vertically pointing Doppler radar data to evaluate the model's shortcomings. Comparisons at a number of geographically diverse sites such as the SGP and the tropical western Pacific (TWP) ARM sites, and at three CloudNet European sites, may be used to isolate differences between convectively and synoptically generated ice cloud microphysical properties. Opportunity also exists to derive global distributions of V_m from spaceborne radar reflectivity measurements. With them, the ratio of the mass to reflectivity-weighted ice particle fall speeds is found to be about 0.8. Opportunity now exists to evaluate them from geographically diverse, ground-based, vertically pointing Doppler radar measurements at multiple radar wavelengths.

Acknowledgments. The authors wish to thank the crew of the NCAR C130 aircraft for the collection of data during AIRS-2, and to John Hallett and Jeffrey Stith for access to it. The authors also wish to thank Carl Schmitt for reviewing the manuscript and Nancy Knight for editing it. Nicolas Gaussiat is thanked for assistance in the data extraction and analysis. This research was supported in part by the NASA CRYSTAL FACE program and MidCiX through NASA-NSF Agreement W-10, 024, and Grant NNG04GF31G, Hal Maring, Program Manager, the CloudSat Project Office, Deborah Vane, Deputy Project Scientist, and the SRON Program Bureau External Research (EO-083).

REFERENCES

Bohren, C. F., and D. R. Huffman, 1983: *Absorption and Scattering of Light by Small Particles*. Wiley & Sons, 530 pp.

Brown, P. R. A., and P. N. Francis, 1995: Improved measurements of the ice water content in cirrus using a total-water probe. *J. Atmos. Oceanic Technol.,* **12,** 410–414.

Bushell, G. C., Y. D. Yan, D. Woodfield, J. Raper, and A. Amal, 2002: On techniques for the measurement of the mass fractal dimension of aggregates. *Adv. Colloid Interface Sci.,* **95,** 1–50.

Donovan, D. P., M. Quante, I. Schlimme, and A. Macke, 2004: Use of equivalent spheres to model the relation between radar reflectivity and optical extinction of ice cloud particles. *Appl. Opt.,* **43,** 4929–4940.

Field, P. R., R. J. Hogan, P. R. A. Brown, A. J. Illingworth, T. W. Choularton, and R. J. Cotton, 2005: Parametrization of ice-particle size distributions for mid-latitude stratiform cloud. *Quart. J. Roy. Meteor. Soc,* **131,** 1997–2017.

——, A. J. Heymsfield, and A. Bansemer, 2006: Shattering and particle interarrival times measured by optical array probes in ice clouds. *J. Atmos. Sci.,* **23,** 1357–1371.

Heymsfield, A. J., and L. J. Donner, 1990: A scheme for parameterizing ice cloud water content in general circulation models. *J. Atmos. Sci.,* **47,** 1865–1877.

——, and J. Iaquinta, 2000: Cirrus crystal terminal velocities. *J. Atmos. Sci.,* **57,** 916–938.

——, and L. M. Miloshevich, 2003: Parameterizations for the cross-sectional area and extinction of cirrus and stratiform ice cloud particles. *J. Atmos. Sci.,* **60,** 936–956.

——, A. Bansemer, P. R. Field, S. L. Durden, J. Stith, J. E. Dye, W. Hall, and T. Grainger, 2002: Observations and parameterizations of particle size distributions in deep tropical cirrus and stratiform precipitating clouds: Results from in situ observations in TRMM field campaigns. *J. Atmos. Sci.,* **59,** 3457–3491.

——, ——, C. G. Schmitt, C. Twohy, and M. R. Poellet, 2004: Effective ice particle densities derived from aircraft data. *J. Atmos. Sci.,* **61,** 982–1003.

——, Z. Wang, and S. Matrosov, 2005: Improved radar ice water content retrieval algorithms using coincident microphysical and radar measurements. *J. Appl. Meteor.,* **44,** 1391–1412.

——, A. Bansemer, and C. Twohy, 2007: Refinements to ice particle mass dimensional and terminal velocity relationships for ice clouds: Part I: Temperature dependence. *J. Atmos. Sci.,* **64,** 1047–1067.

Hong, S.-J., J. Dudhia, and S.-H. Chen, 2004: A revised approach to ice microphysical processes for the bulk parameterization of clouds and precipitation. *Mon. Wea. Rev.,* **132,** 103–120.

Iacobellis, S. F., G. M. McFarquhar, D. L. Mitchell, and R. C. J. Somerville, 2003: The sensitivity of radiative fluxes to parameterized cloud microphysics. *J. Climate,* **16,** 2979–2996.

Isaac, G. A., and Coauthors, 2005: First results from the Alliance Icing Research Study II. *Proc. 43d Aerospace Science Meeting and Exhibit,* Reno Nevada, AIAA, AIAA-2005-0252.

Jakob, C., 2002: Ice clouds in numerical weather prediction models—Progress, problems and prospects. *Cirrus,* D. Lynch et al., Eds, Oxford University Press, 327–345.

Lawson, R. P., B. Baker, B. Pilson, and Q. Mo, 2006: In situ observations of the microphysical properties of wave, cirrus, and anvil Clouds. Part II: Cirrus clouds. *J. Atmos. Sci.,* **63,** 3160–3185.

Li, L., and Coauthors, 2001: Retrieval of atmospheric attenuation using combined ground-based and airborne 95-GHz cloud radar measurements. *J. Atmos. Oceanic Technol.,* **18,** 1345–1353.

Lin, Y.-L., R. D. Farley, and H. D. Orville, 1983: Bulk parameterization of the snow field in a cloud model. *J. Climate Appl. Meteor.,* **22,** 1065–1092.

Locatelli, J. D., and P. V. Hobbs, 1974: Fall speeds and masses of solid precipitation particles. *J. Geophys. Res.,* **79,** 2185–2197.

Lohmann U., and B. Kärcher, 2002: First interactive simulations of cirrus clouds formed by homogeneous freezing in the ECHAM general circulation model. *J. Geophys. Res.,* **107,** 4105, doi:10.1029/2001JD000767.

Matrosov, S. Y., 1998: A dual-wavelength radar method to measure snowfall rate. *J. Appl. Meteor.,* **37,** 1510–1521.

——, and A. J. Heymsfield, 2000: The use of Doppler radar measurements to derive ice cloud particle fall velocity relations for climate models. *J. Geophys. Res.,* **105,** 22 427–22 436.

——, ——, and Z. Wang, 2005: Dual-frequency radar ratio of nonspherical atmospheric hydrometeors. *Geophys. Res. Lett.,* **32,** L13816, doi:10.1029/2005GL023210.

Mitchell, D. L., and A. J. Heymsfield, 2005: Refinements in the treatment of ice particle terminal velocities, highlighting aggregates. *J. Atmos. Sci.,* **62,** 1637–1644.

Orr, B. W., and R. A. Kropfli, 1999: A method for estimating particle fall velocities from vertically pointing Doppler radar. *J. Atmos. Oceanic Technol.,* **16,** 29–37.

Rutledge, S. A., and P. V. Hobbs, 1984: The mesoscale and microscale structure and organization of clouds and precipitation in midlatitude cyclones. XII: A diagnostic modeling study of precipitation development in narrow cold-frontal rainbands. *J. Atmos. Sci.,* **41,** 2949–2972.

Westbrook, C. D., R. C. Ball, P. R. Field, and A. J. Heymsfield, 2004: Theory of growth by differential sedimentation, with application to snowflake formation. *Phys. Rev. E,* **70,** 021403, doi:10.1103/PhysRevE.70.021403.